

LETTER TO THE EDITOR

TMC-1, the starless core sulfur factory: Discovery of NCS, HCCS, H₂CCS, H₂CCCS, and C₄S and detection of C₅S^{*}

J. Cernicharo¹, C. Cabezas¹, M. Agúndez¹, B. Tercero^{2,3}, J. R. Pardo¹, N. Marcelino¹, J.D. Gallego³, F. Tercero³, J.A. López-Pérez³, and P. de Vicente³,

¹ Grupo de Astrofísica Molecular, Instituto de Física Fundamental (IFF-CSIC), C/ Serrano 121, 28006 Madrid, Spain.
e-mail: : jose.cernicharo@csic.es

² Observatorio Astronómico Nacional (IGN), C/ Alfonso XII, 3, 28014, Madrid, Spain.

³ Centro de Desarrollos Tecnológicos, Observatorio de Yebes (IGN), 19141 Yebes, Guadalajara, Spain.

Received; accepted

ABSTRACT

We report the detection of the sulfur-bearing species NCS, HCCS, H₂CCS, H₂CCCS, and C₄S for the first time in space. These molecules were found towards TMC-1 through the observation of several lines for each species. We also report the detection of C₅S for the first time in a cold cloud through the observation of five lines in the 31–50 GHz range. The derived column densities are $N(\text{NCS}) = (7.8 \pm 0.6) \times 10^{11} \text{ cm}^{-2}$, $N(\text{HCCS}) = (6.8 \pm 0.6) \times 10^{11} \text{ cm}^{-2}$, $N(\text{H}_2\text{CCS}) = (7.8 \pm 0.8) \times 10^{11} \text{ cm}^{-2}$, $N(\text{H}_2\text{CCCS}) = (3.7 \pm 0.4) \times 10^{11} \text{ cm}^{-2}$, $N(\text{C}_4\text{S}) = (3.8 \pm 0.4) \times 10^{10} \text{ cm}^{-2}$, and $N(\text{C}_5\text{S}) = (5.0 \pm 1.0) \times 10^{10} \text{ cm}^{-2}$. The observed abundance ratio between C₃S and C₄S is 340, that is to say a factor of approximately one hundred larger than the corresponding value for CCS and C₃S. The observational results are compared with a state-of-the-art chemical model, which is only partially successful in reproducing the observed abundances. These detections underline the need to improve chemical networks dealing with S-bearing species.

Key words. Astrochemistry — ISM: molecules — ISM: individual (TMC-1) — line: identification — molecular data

1. Introduction

The cold dark core TMC-1 presents an interesting carbon-rich chemistry that leads to the formation of long neutral carbon-chain radicals and their anions, as well as cyanopolyynes (see Cernicharo et al. 2020a,b and references therein). The carbon chains CCS and CCCS are particularly abundant in this cloud (Saito et al. 1987; Yamamoto et al. 1987) and also exist in the envelopes of carbon-rich circumstellar envelopes (Cernicharo et al. 1987). TMC-1 is also peculiar due to the presence of protonated species of abundant large carbon chains such as HC₃O⁺ (Cernicharo et al. 2020c), HC₅NH⁺ (Marcelino et al. 2020), HC₃S⁺ (Cernicharo et al. 2021a), and CH₃CO⁺ (Cernicharo et al. 2021b). The number of sulfur-bearing species detected to date in TMC-1 is small compared to oxygen- and nitrogen-bearing species (see, e.g. McGuire et al. 2019). In fact, the chemistry of sulfur-bearing molecules is strongly dependent on the depletion of sulfur (Vidal et al. 2017). Many reactions involving S⁺ with neutrals as well as radicals with S and CS have to be studied to achieve a better chemical modelling of sulfur-bearing species (Petrie 1996; Bulut et al. 2021). Nevertheless, the main input to understand these chemical processes is to unveil new sulfur-bearing species in the interstellar medium as well as to under-

stand their formation paths and their role in the chemistry of sulfur.

In this letter we report the discovery, for the first time in space, of the following five new sulfur-bearing species: NCS, HCCS, H₂CCS, H₂CCCS, and C₄S. The detection of C₅S in a cold dark cloud is also reported for the first time. A detailed observational study of the most relevant S-bearing species in this cloud is accomplished. We discuss these results in the context of state-of-the-art chemical models.

2. Observations

New receivers, built within the Nanocosmos project¹, and installed at the Yebes 40m radio telescope were used for the observations of TMC-1. The receivers and the spectrometers have been described by Tercero et al. (2021). The observations needed to complete the Q-band line survey towards TMC-1 ($\alpha_{J2000} = 4^{\text{h}}41^{\text{m}}41.9^{\text{s}}$ and $\delta_{J2000} = +25^{\circ}41'27.0''$) were performed in several sessions during December 2019 and January 2021. All data were analysed using the GILDAS package². The observing procedure has been previously described (see, e.g. Cernicharo et al. 2021a,b). The IRAM 30m data come from a line survey performed towards TMC-1 and B1 and the observations have been described by Marcelino et al. (2007) and Cernicharo et al. (2013).

The intensity scale, antenna temperature (T_A^*) was calibrated using two absorbers at different temperatures and an atmospheric transmission model (ATM; Cernicharo 1985; Pardo et al. 2001). Calibration uncertainties have been adopted to be 10 %. The

^{*} Based on observations carried out with the Yebes 40m telescope (projects 19A003, 20A014, and 20D023) and the Institut de Radioastronomie Millimétrique (IRAM) 30m telescope. The 40m radiotelescope at Yebes Observatory is operated by the Spanish Geographic Institute (IGN, Ministerio de Transportes, Movilidad y Agenda Urbana). IRAM is supported by INSU/CNRS (France), MPG (Germany), and IGN (Spain).

¹ <https://nanocosmos.iff.csic.es/>

² <http://www.iram.fr/IRAMFR/GILDAS>

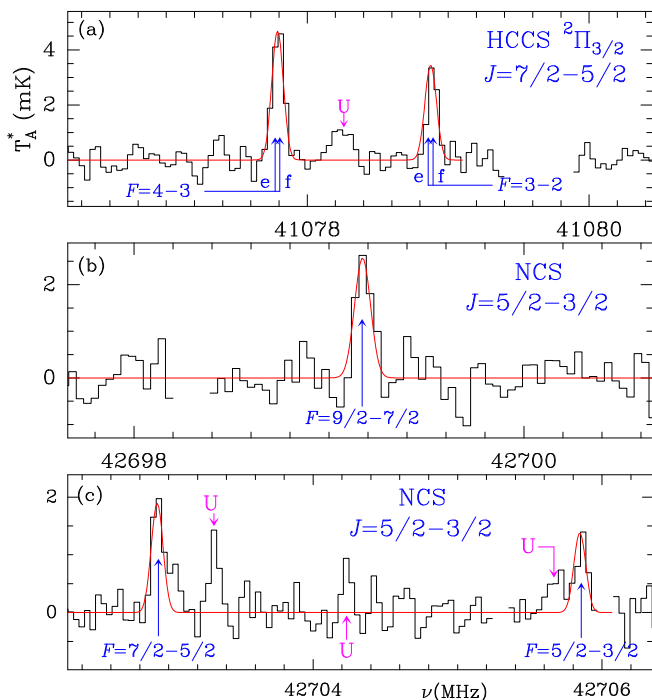


Fig. 1. Observed lines of HCCS (panel *a*) and NCS (panels *b* and *c*) towards TMC-1. The abscissa corresponds to the rest frequency assuming a local standard of rest velocity of the source of 5.83 km s^{-1} (see text). Blanked channels correspond to negative features produced in the frequency switching data folding. The ordinate is the antenna temperature corrected for atmospheric and telescope losses in milliKelvin. Spectral resolution is 38.15 kHz . The red lines show the synthetic spectrum of HCCS and NCS for a rotational temperature of 5 K , a linewidth of 0.6 km s^{-1} , and a column density of $6.8 \times 10^{11} \text{ cm}^{-2}$ and $7.8 \times 10^{11} \text{ cm}^{-2}$, respectively.

nominal spectral resolution of 38.15 kHz was used for the final spectra.

3. Results and discussion

Line identification in our TMC-1 survey has been performed using the MADEX catalogue (Cernicharo 2012), the Cologne Database of Molecular Spectroscopy catalogue (Müller et al. 2005), and the JPL catalogue (Pickett 1998). A description of the methods used to fit the data and to derive column densities is provided in Appendix A.

3.1. HCCS and NCS

Among the unidentified spectral features, we have found a couple separated by 1 MHz that perfectly match the frequencies of the strongest hyperfine components of the $J=7/2-5/2$ transition of HCCS ($^2\Pi_{3/2}$). This species was observed in the laboratory by Kim et al. (2002) and the prediction of its rotational spectrum is available in the CDMS (Müller et al. 2005) and MADEX (Cernicharo 2012) catalogues. Taking into account the perfect match in frequencies, the narrow linewidth of the emission features in this source, and the perfect match in the relative intensities of the two hyperfine components, the possibility of a fortuitous coincidence is very low. Hence, we conclude that these two lines arise from HCCS. The observed lines are shown in Fig. 1 and the derived line parameters are given in Table D.1. The synthetic spectrum on Fig. 1 corresponds to $T_r=5 \text{ K}$ and $N(\text{HCCS}) = 6.8 \times 10^{11} \text{ cm}^{-2}$. We searched for HCCS but only a 3σ upper

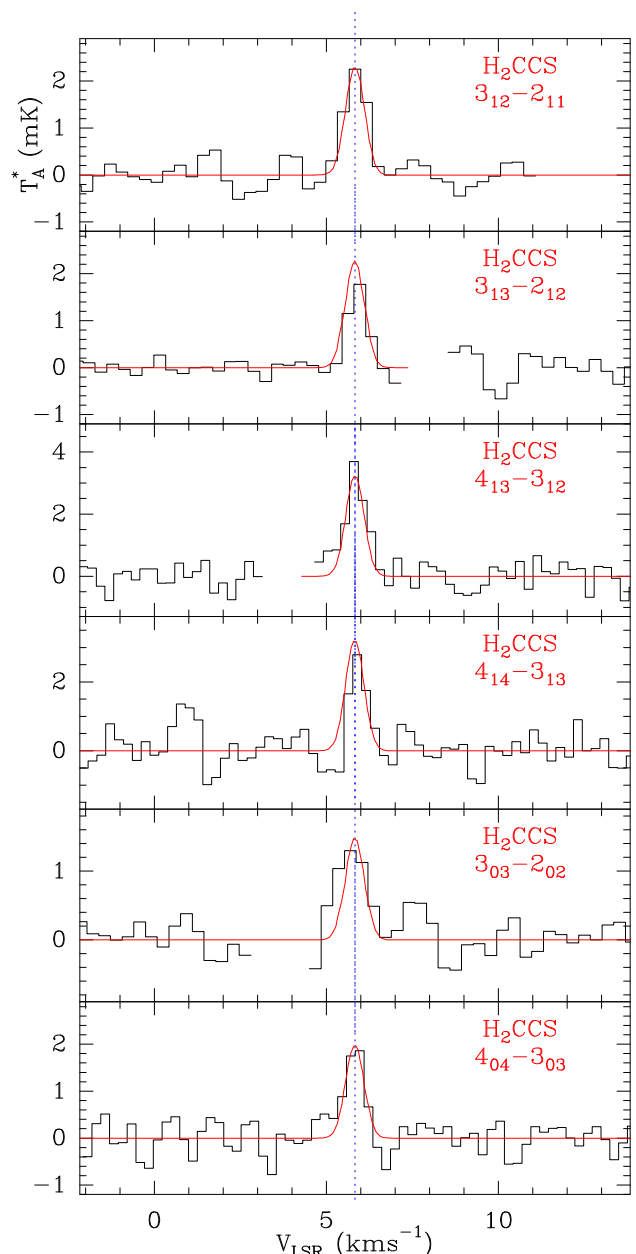


Fig. 2. Observed transitions of H_2CCS towards TMC-1. The abscissa corresponds to the velocity in km s^{-1} of the source with respect to the local standard of rest. Line parameters are given in Table D.1. The ordinate is the antenna temperature corrected for atmospheric and telescope losses in milliKelvin. Blanked channels correspond to negative features produced by the folding of the frequency switching observations. The vertical blue dashed line indicates the v_{LSR} of the cloud (5.83 km s^{-1}). The red line spectra correspond to the synthetic model spectrum for each line adopting $T_r=7 \text{ K}$, $N(o\text{-H}_2\text{CCS}) = 6.0 \times 10^{11} \text{ cm}^{-2}$, and $N(p\text{-H}_2\text{CCS}) = 1.8 \times 10^{11} \text{ cm}^{-2}$ (see text).

limit to its column density of $2.4 \times 10^{11} \text{ cm}^{-2}$ can be given (see Table 1).

Thiocyanogen, NCS, has been observed in the laboratory (Amamo & Amano 1991; McCarthy et al. 2003; Maeda et al. 2007), but never detected in space. Only one rotational transition lies within the Q-band, the $J=5/2-3/2$ transition of NCS in its $^2\Pi_{3/2}$ ladder. Figure 1 shows the three hyperfine components of this transition observed in TMC-1. The match between observations and the synthetic spectrum, corresponding to $T_r=5 \text{ K}$ and $N(\text{NCS}) = 7.8 \times 10^{11} \text{ cm}^{-2}$, is remarkably good, ensuring the dis-

covery of this sulfur compound in TMC-1. The oxygen analogue of thiocyanogen, the isocyanate radical (NCO), was detected in cold core L483 by Marcelino et al. (2018). Unfortunately, NCO does not have lines in the 31-50 GHz range.

3.2. H_2CCS and H_2CCCS

Prompted by the detection of HCCS, we searched for other sulfur-bearing species in our survey. McGuire et al. (2019) searched for H_2CCS , thioketene, in TMC-1. They obtained an upper limit to its column density of $5.5 \times 10^{12} \text{ cm}^{-2}$. Unfortunately they used a transition with an upper level energy around 40 K, which is not the best for the physical conditions of TMC-1. In this work we report the discovery of thioketene in space through observations of transitions with smaller upper level energies.

Spectroscopic laboratory data of thioketene (Georgiou et al. 1979; Winnewiser & Schäfer 1980; McNaughton et al. 1996) and H_2CCCS (Brown et al. 1988) were used to predict the frequencies of these species and implement them in the MADEx code. The dipole moments adopted for H_2CCS and H_2CCCS are 1.02 D (Georgiou et al. 1979) and 2.06 D (Brown et al. 1988), respectively. We detected the four ortho and two para transitions of H_2CCS expected in our data, as shown in Fig. 2. For H_2CCCS (propadienethione), six ortho and three para transitions are detected (see seven of them in Fig. 3). The derived line parameters for both species are given in Table D.1.

An analysis of the data through a standard rotation diagram provides rotational temperatures of 7 ± 1 K and 10 ± 1 K for H_2CCS and H_2CCCS , respectively. For H_2CCS , we derived $N(\text{ortho}) = (6.0 \pm 0.6) \times 10^{11} \text{ cm}^{-2}$ and $N(\text{para}) = (1.8 \pm 0.2) \times 10^{11} \text{ cm}^{-2}$. Hence, the ortho/para ratio for this species is 3.3 ± 0.7 . For H_2CCCS , we derived $N(\text{ortho}) = (3.0 \pm 0.3) \times 10^{11} \text{ cm}^{-2}$ and $N(\text{para}) = (6.5 \pm 0.5) \times 10^{10} \text{ cm}^{-2}$, respectively. The ortho/para abundance ratio derived for this species is 4.6 ± 0.8 . These ortho/para ratios are compatible with the 3/1 value expected from the statistical spin degeneracies. They imply that non-significant enrichment of the para species is produced through reactions of H_2CCS and H_2CCCS with H_3^+ , or other protonated molecular cations. The synthetic spectrum computed with these parameters for both species is shown in red in the different panels of Figures 2 and 3. The derived abundance ratio between H_2CCS and H_2CCCS is ≈ 2 , which is very different from the H_2CCO/H_2CCCO abundance ratio of > 130 derived in the same source by Cernicharo et al. (2020c), but very similar to the C_2S/C_3S abundance ratio of ~ 3 derived here (see Table 1).

3.3. C_4S and C_5S

Taking the large column density derived for CCS and C_3S into account (Cernicharo et al. 2021a), the next member of this family, C_4S , is a potential candidate to be present in TMC-1. The spectroscopic laboratory data used to predict the spectrum of C_4S are from Hirahara et al. (1993) and Gordon et al. (2001). A dipole moment of 4.03 D was computed through ab initio calculations by Pascoli & Lavendy (1998) and Lee (1997). Nineteen transitions of this species have frequencies within the range of our line survey. The line by line search through our data provides a clear detection for the $N_u=10$ up to 13, $J_u=N_u+1$ transitions (see Fig. B.1). A rotational temperature of 7 ± 1 K was derived from these lines. The model fitting method (see Appendix A) was used to derive a column density of $(3.8 \pm 0.4) \times 10^{10} \text{ cm}^{-2}$. The stacked spectrum obtained for these lines and for the weaker

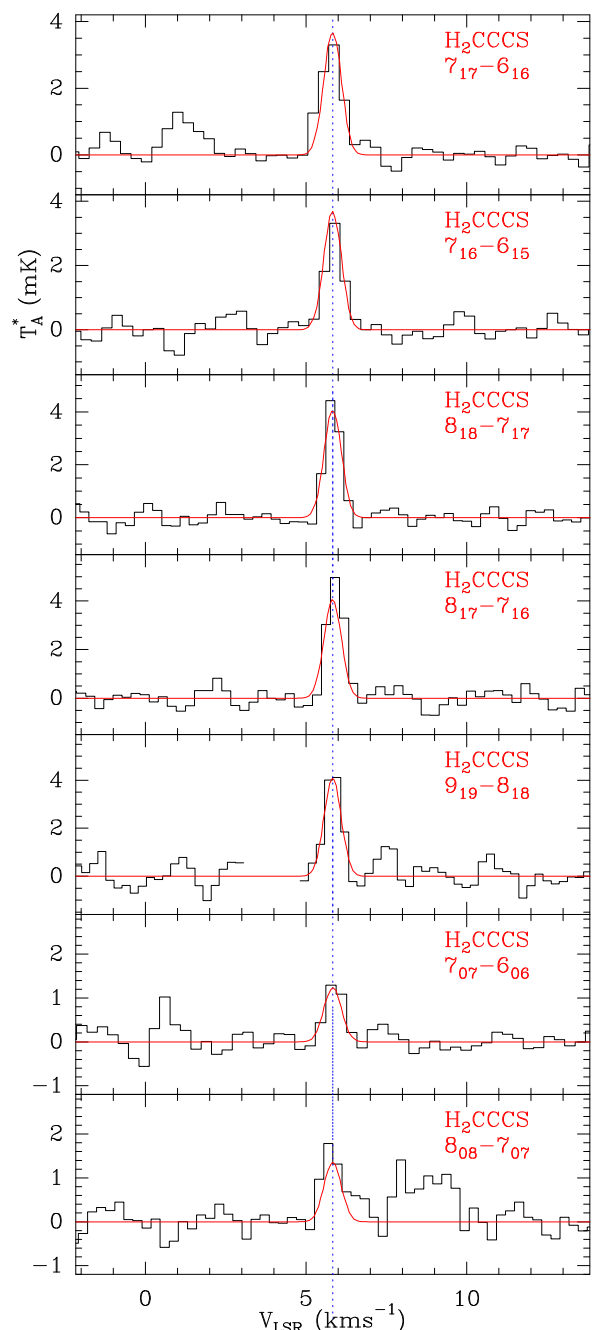


Fig. 3. Selected transitions of H_2CCCS towards TMC-1. The abscissa corresponds to the velocity in km s^{-1} of the source with respect to the local standard of rest. Line parameters are given in Table D.1. The ordinate is the antenna temperature corrected for atmospheric and telescope losses in milliKelvin. Blanked channels correspond to negative features produced by the folding of the frequency switching observations. The vertical blue dashed line indicates the v_{LSR} of the cloud (5.83 km s^{-1}). The red line spectra correspond to the synthetic model of the emission obtained for $T_r=10 \text{ K}$, $N(o\text{-}H_2CCS) = 3.0 \times 10^{11} \text{ cm}^{-2}$, and $N(p\text{-}H_2CCS) = 6.5 \times 10^{10} \text{ cm}^{-2}$.

$J_u=N$ and $J_u=N-1$ transitions are shown in panels (b) and (c) of Fig. B.1, respectively.

The next member of the C_nS family, C_5S , was tentatively detected towards the carbon-rich star CW Leo by Bell et al. (1993) and confirmed by Agúndez et al. (2014). Laboratory spectroscopy from Gordon et al. (2001) and a dipole moment of 4.65 D (Pascoli & Lavendy 1998) have been adopted. Five

Table 1. Column densities of sulfur-bearing species in TMC-1.

Molecule	T_{rot} (K)	N_{obs} (cm $^{-2}$)	N_{calc} (cm $^{-2}$) ^e
CS ^{a*}	10.0	$(3.50 \pm 0.40) \times 10^{14}$	3.1×10^{14}
C ³⁴ S [*]	10.0	$(1.45 \pm 0.10) \times 10^{13}$	
¹³ C ³⁴ S [*]	10.0	$(1.45 \pm 0.20) \times 10^{11}$	
HCS	5.0 ^b	$(5.50 \pm 0.50) \times 10^{12}$	5.1×10^{10}
HSC	5.0 ^b	$(1.30 \pm 0.20) \times 10^{11}$	
NCS	5.0 ^b	$(7.80 \pm 0.60) \times 10^{11}$	2.5×10^{10}
HCCS	5.0 ^b	$(6.80 \pm 0.60) \times 10^{11}$	3.1×10^{10}
H ₂ CS ^c	10.0	$(4.70 \pm 0.40) \times 10^{13}$	9.5×10^{12}
H ₂ C ³⁴ S ^c	10.0	$(1.80 \pm 0.18) \times 10^{12}$	
<i>o</i> -H ₂ CCS	7.0 \pm 1.0	$(6.00 \pm 0.60) \times 10^{11}$	1.8×10^{12}
<i>p</i> -H ₂ CCS	7.0 \pm 1.0	$(1.80 \pm 0.20) \times 10^{11}$	
<i>o</i> -H ₂ CCCS	10.0 \pm 1.0	$(3.00 \pm 0.30) \times 10^{11}$	7.8×10^{10}
<i>p</i> -H ₂ CCCS	10.0 \pm 1.0	$(6.50 \pm 0.60) \times 10^{10}$	
CCS [*]	5.1 \pm 0.2	$(5.50 \pm 0.65) \times 10^{13}$	3.8×10^{11}
CC ³⁴ S [*]	3.6 \pm 0.4	$(5.00 \pm 0.50) \times 10^{12}$	
CCCS [*]	5.8 \pm 0.2	$(1.30 \pm 0.13) \times 10^{13}$	1.1×10^{13}
CCC ³⁴ S [*]	6.7 \pm 0.2	$(5.30 \pm 0.50) \times 10^{11}$	
C ₄ S	7.0 \pm 1.0	$(3.80 \pm 0.50) \times 10^{10}$	1.6×10^{10}
C ₅ S	7.0 \pm 1.0	$(5.00 \pm 1.00) \times 10^{10}$	1.9×10^{11}
HCS ⁺⁺	10.0	$(1.00 \pm 0.10) \times 10^{13}$	1.7×10^{11}
HC ³⁴ S ⁺⁺	10.0	$(7.10 \pm 0.70) \times 10^{11}$	
HC ₃ S ⁺⁺	10.0 \pm 2.0	$(4.00 \pm 1.50) \times 10^{11}$	2.8×10^{11}
HSCN	5.0	$(5.80 \pm 0.60) \times 10^{11}$	3.7×10^9
HNCS	5.0	$(3.80 \pm 0.40) \times 10^{11}$	1.2×10^{10}
HC ₃ S ^d	5.0	$\leq 2.40 \times 10^{11}$	1.5×10^{11}
HCNS ^d	10.0	$\leq 6.00 \times 10^{10}$	3.9×10^6
HSNC ^d	10.0	$\leq 2.00 \times 10^{10}$	
HSCS ^{++d}	5.0	$\leq 4.00 \times 10^{12}$	
HCCSH ^d	7.0	$\leq 3.00 \times 10^{12}$	
HCCCSH ^d	7.0	$\leq 2.40 \times 10^{11}$	

Notes.

Entries in bold face correspond to the molecular species detected for the first time in space, or in TMC-1 (C₅S).

(*) Data from Cernicharo et al. (2021a).

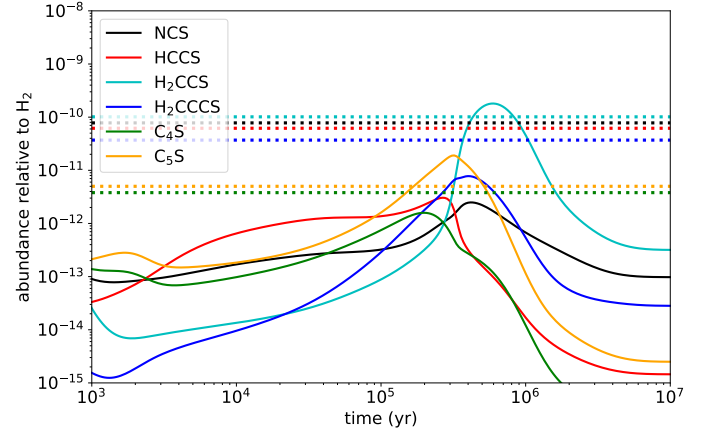
(a) Derived from C³⁴S and the C₃S/C₃³⁴S abundance ratio.

(b) Rotational temperature assumed identical to that of CCS.

(c) Column density refers to the ortho or para species. Assuming an ortho/para ratio of 3, the total column density can be estimated by multiplying the para value by a factor of 4.

(d) Upper limits correspond to 3 σ values derived assuming the indicated rotational temperature and a linewidth of 0.6 km s⁻¹.

(e) Maximum fractional abundance calculated in the 10⁵-10⁶ yr range was converted to column density using $N(\text{H}_2) = 10^{22}$ cm⁻² (Cernicharo & Guélin 1987).

**Fig. 4.** Calculated fractional abundances of the six S-bearing species reported in this work as a function of time. Horizontal dotted lines correspond to observed values in TMC-1 adopting a column density of H₂ of 10²² cm⁻² (Cernicharo & Guélin 1987).**3.4. Chemical models**

The chemistry of sulfur-bearing molecules in cold dark clouds was recently discussed by Vidal et al. (2017), Vastel et al. (2018), and Laas & Caselli (2019), based on new chemical network developments. These studies revealed that the chemistry of sulfur strongly depends on the poorly constrained degree of depletion of this element in cold dense clouds. Chemical networks are relatively incomplete when dealing with S-bearing species. For example, from the six species detected in this work, only C₄S is included in the chemical networks RATE12 (UMIST; McElroy et al. 2013) and kida.uva.2014 (KIDA; Wakelam et al. 2015). Vidal et al. (2017) made an effort to expand the number of reactions involving S-bearing species significantly by including several of the molecules reported here. These authors, however, discussed only a small number of sulfur compounds and did not provide calculated abundances for any of the six species reported in this work. We therefore carried out chemical modelling calculations to describe the chemistry of the new sulfur-bearing molecules detected. We used the gas-phase chemical network RATE12 from the UMIST database (McElroy et al. 2013), expanded with the set of gas-phase reactions involving S-bearing species constructed by Vidal et al. (2017). We included additional reactions to describe the chemistry of NCS and C₅S, which was not treated by Vidal et al. (2017), assuming a similar chemical kinetics behaviour to NCO and C₃S, respectively (see Table E.1). Our main purpose is to see whether state-of-the-art gas-phase chemical networks can explain the abundances of the S-bearing species discovered. We adopted typical parameters of cold dark clouds: a gas kinetic temperature of 10 K, a volume density of H₂ of 2×10^4 cm⁻³, a visual extinction of 30 mag, a cosmic-ray ionisation rate of H₂ of 1.3×10^{-17} s⁻¹, and 'low-metal' elemental abundances (see, e.g. Agúndez & Wakelam 2013). We therefore adopted a relatively low gas-phase abundance of sulfur, 8×10^{-8} relative to H.

Calculated column densities for S-bearing species are compared with observed values in Table 1. In Fig. 4 we compare the abundances calculated for the six S-bearing species detected in this study with the values derived from the observations. The peak abundances calculated are within one order of magnitude of the observed abundance for H₂CCS, H₂CCCS, C₄S, and C₅S. The two species for which the chemical model severely disagrees with observations are NCS and HCCS, in which case calculated

lines from $J_u=17$ up to 21 have been detected (see Fig. B.2). The model fitting provides a rotational temperature of 7 ± 2 K and a column density of $(5.0 \pm 1.0) \times 10^{10}$ cm⁻². The abundance ratio between C₄S and C₅S is of the order of unity, and the abundance ratio C₂S/C₃S/C₄S/C₅S is 5500/1300/3.8/5.0. The change in abundance for C₄S and C₅S relative to C₂S is of three orders of magnitude. This result is very different than the one obtained by Agúndez et al. (2014) for the carbon-rich star IRC+10216. In this object, the derived C₃S/C₅S ratio is ~ 1 -10 (depending on the assumed rotational temperature), versus ~ 260 in TMC-1. However, the C₂S/C₃S abundance ratio is the same for both sources, that is to say ~ 3 . The radical C₄S has not been detected yet in IRC+10216 (Agúndez et al. 2014). S-bearing carbon chains do not follow the smooth decrease in abundance observed in cold dark clouds and circumstellar envelopes for other carbon chains such as cyanopolynes (HC_{2n+1}N; a factor 3-5 between members of this molecular species).

abundances are lower than observed by more than one order of magnitude. These two species have low calculated abundances because they are assumed to react quickly with O atoms, with rate coefficients $\geq 10^{-10} \text{ cm}^3 \text{ s}^{-1}$. This same behaviour has been previously found for other radicals detected in cold dark clouds such as HCCO (Agúndez et al. 2015) and C_2S (Cernicharo et al. 2021a; see also Table 1). In these cases, the fast destruction with neutral atoms, including O, resulted in calculated abundances well below the observed values. These facts suggest that either the abundance of O atoms calculated by gas-phase chemical models of cold clouds is too high or O atoms are not as reactive with certain radicals as currently thought. While the low-temperature reactivity of O atoms with closed-shell S-bearing species such as CS has been shown to be low (Bulut et al. 2021), its reactivity with radicals is very poorly known.

The radical NCS is formed in the chemical model through the reactions $\text{CN} + \text{SO}$ and $\text{N} + \text{HCS}$. The kinetics and product distribution of these reactions is, however, largely unconstrained. This uncertainty also affects the chemical network involving the family of CHNS isomers, for which the chemical model underestimates the column densities (see Table 1). In the chemical models of dark clouds performed by Adande et al. (2010) and Vidal et al. (2017), the main formation pathways to these molecules involve grain surface reactions, which are not included in our chemical network.

The formation of the other five molecules reported in this work, which are S-bearing carbon chains and thus can be represented by the formula $\text{H}_m\text{C}_n\text{S}$, occurs through two types of chemical routes. The first one involves neutral-neutral reactions. Along this pathway, HCCS is formed by the reactions $\text{C} + \text{H}_2\text{CS}$ and $\text{OH} + \text{C}_3\text{S}$, the reaction $\text{S} + \text{C}_2\text{H}_3$ yields H_2CCS , while H_2CCCS is mostly formed by the reaction $\text{S} + \text{CH}_2\text{CCH}$. On the other hand, the carbon chain C_4S is formed through the reactions $\text{S} + \text{C}_4\text{H}$ and $\text{C} + \text{HC}_3\text{S}$, while C_5S is produced in the reactions $\text{C}_4\text{H} + \text{CS}$ and $\text{S} + \text{C}_5\text{H}$. It must be noted that the kinetics and product distribution of these reactions is very poorly known. Most of these reactions are assumed to proceed with capture rate coefficients by Vidal et al. (2017).

The second pathway consists of reactions involving cations, which ultimately lead to the ion $\text{H}_p\text{C}_n\text{S}^+$, which dissociatively recombines with electrons to yield $\text{H}_m\text{C}_n\text{S}$, where typically $p = m + 1$. In this route, the ions H_2CCS^+ , H_3CCCS^+ , HC_4S^+ , and HC_5S^+ are the precursors of HCCS, H_2CCS , H_2CCCS , C_4S , and C_5S , respectively. The abovementioned ions are in turn formed through reactions between atomic S with hydrocarbon ions and S^+ with neutral hydrocarbons. In the same line of the reactions discussed above, there are large uncertainties regarding these reactions, for which rate coefficients and product distributions are taken from Vidal et al. (2017). The chemical network is probably incomplete in that it misses important reactions involving S and S^+ . Moreover, reactions on grain surfaces, which are considered by Vidal et al. (2017) but are not taken into account here, could play an important role.

4. Conclusions

In this work, we present the detection of five new sulfur-bearing molecules in TMC-1: NCS, HCCS, H_2CCS , H_2CCCS , and C_4S . In addition, the species C_5S previously found only towards carbon-rich circumstellar envelopes is also detected in a cold dark cloud for the first time. Chemical models fail to reproduce the observed column densities which implies that the chemical networks are incomplete and that laboratory and theoretical work

has to be performed in order to understand the chemistry of sulfur in cold prestellar cores.

Acknowledgements. The Spanish authors thank Ministerio de Ciencia e Innovación for funding support through projects AYA2016-75066-C2-1-P, PID2019-106235GB-I00 and PID2019-107115GB-C21 / AEI / 10.13039/501100011033, and grant RyC-2014-16277. We also thank ERC for funding through grant ERC-2013-Syg-610256-NANOCOSMOS.

References

- Adande, G.R., Halfen, D.T., Ziurys, L.M., et al. 2010, *ApJ*, 725, 561
 Agúndez, M. & Wakelam, V. 2013, *Chem. Rev.*, 113, 8710
 Agúndez, M., Cernicharo, J., & Guélin, M. 2014, *A&A*, 570, A45
 Agúndez, M., Cernicharo, J., & Guélin, M. 2015, *A&A*, 577, L5
 Agúndez, M., Marcelino, N., Cernicharo, J., & Tafalla, M. 2018, *A&A*, 611, L1
 Amano, Takayoshi & Amano Takako 1991, *J. Chem. Phys.*, 95, 2275
 Bell, M.B., Avery, L.W., Feldman, P.A., 1993, *ApJ*, 417, L37
 Brown, R.D., Godfrey, P.D., Champion, R., Woodruff, M., 1982, *Aust. J. Chem.*, 35, 1747
 Brown, R.D., Dyall, K.G., Elmes, P.S., et al., 1988, *J. Am. Chem. Soc.*, 110, 789
 Bulut, N., Roncero, O., Aguado, A., et al. 2021, *A&A*, 646, A5
 Cabezas, C., Endo, Y., Roueff, E., et al. 2021, *A&A*, 646, L1
 Crabtree, K.N., Martin-Drumel, M.-A., Brown, G.G., et al., 2016, *J. Chem. Phys.*, 144, 124201
 Cernicharo, J. 1985, Internal IRAM report (Granada: IRAM)
 Cernicharo, J. & Guélin, M. 1987, *A&A*, 176, 299
 Cernicharo, J., Guélin, M., Hein, H., Kahane, C., 1987, *A&A*, 181, L9
 Cernicharo, J., 2012, in *ECLA 2011: Proc. of the European Conference on Laboratory Astrophysics*, EAS Publications Series, 2012, Ed.: C. Stehl, C. Joblin, & L. d'Hendecourt (Cambridge: Cambridge Univ. Press), 251; https://nanocosmos.iff.csic.es/?page_id=1619
 Cernicharo, J., Tercero, B., Fuente, A., et al. 2013, *ApJ*, 771, L10
 Cernicharo, J., Cabezas, C., Pardo, J. R., et al. 2019, *A&A*, 630, L2
 Cernicharo, J., Marcelino, N., Pardo, J.R., et al. 2020a, *A&A*, 641, L9
 Cernicharo, J., Marcelino, N., Agúndez, M., et al. 2020b, *A&A*, 642, L8
 Cernicharo, J., Marcelino, N., Agúndez, M., et al. 2020c, *A&A*, 642, L17
 Cernicharo, J., Cabezas, C., Endo, Y., et al. 2021a, *A&A*, 646, L3
 Cernicharo, J., Cabezas, C., Baillieux, S., et al. 2021b, *A&A*, 646, L7
 Cernicharo, J., Cabezas, C., Agúndez, M., et al. 2021c, *A&A*, in press
 Dunning, T. H., 1989, *J. Chem. Phys.*, 90, 1007
 Endo, Y., Kohguchi, H., Ohshima, Y. 1994, *Faraday Discuss.*, 97, 341.
 Fossé, D., Cernicharo, J., Gerin, M., Cox, P. 2001, *ApJ*, 552, 168
 Frerking, M.A., Linke, R.A. & Thaddeus, P. 1979, *ApJ*, 234, L143
 Georgiou, K., Krot, H.W., Landsberg, B.M. 1979, *J. Mol. Spectrosc.*, 77, 365
 Gordon, V.D., McCarthy, M.C., Apponi, A.J., Thaddeus, P. 2001, *ApJS*, 134, 311
 Kaifu, N., Ohishi, M., Kawaguchi, K., et al., 2004, *PASJ*, 56, 69
 Halfen, D.T., Ziurys, L.M., Brünken, S., et al. 2009, *ApJ*, 702, L124
 Hirahara, Y., Ohshima, Y., Endo, Y., 1993 *ApJ*, 408, L113
 Hirahara, Y., Ohshima, Y., Endo, Y., 1994 *J. Chem. Phys.*, 101, 7342
 Kim, E., Habara, H., Yamamoto, S. 2002, *J. Mol. Spectrosc.*, 212, 83
 Laas, J. C. & Caselli, P. 2019, *A&A*, 624, A108
 Lee, S. 1997, *Chem. Phys. Lett.*, 268, 69
 Lee, K.L., Martin-Drumel, M.-A., Lattanzi, V., et al. 2019, *Mol. Phys.*, 117, 1381
 Lique, F., Spielfeld, A., Dubernet, M.L., Feautrier, N. 2005, *J. Chem. Phys.*, 123, 4316
 Lique, F., Cernicharo, J., Cox P. 2006, *ApJ*, 653, 1342
 Loison, J.-C., Agúndez, M., Marcelino, N., et al. 2016, *MNRAS*, 456, 4101
 Maeda, A., Habara, H. & Amano, T. 2007, *Mol. Phys.*, 105, 477
 Marcelino, N., Cernicharo, J., Agúndez, M., et al. 2007, *ApJ*, 665, L127
 Marcelino, N., Agúndez, M., Cernicharo, J. et al., 2018, *A&A*, 612, L10
 Marcelino, N., Agúndez, M., Tercero, B., et al., 2020a, *A&A*, 643, L6
 McElroy, D., Walsh, C., Markwick, A. J., et al. 2013, *A&A*, 550, A36
 McGuire, B.A., Martin-Drumel, M.A., Thorwirth, S., et al. 2010, *Phys. Chem. Chem. Phys.*, 18, 22693
 McGuire, B.A., Shingledecker, C.N., Willis, E.R., et al. 2019, *ApJ*, 883, 201
 McCarthy, M.C., Coosky, A.L., Mohamed, S., et al. 2003, *ApJS*, 144, 287
 McCarthy, M.C., Thaddeus, P., Wilke, J., et al. 2009, *J. Chem. Phys.*, 130, 234304
 Müller, H.S.P., Schlöder, F., Stutzki, J., Winnewisser, G. 2005, *J. Mol. Struct.*, 742, 215
 McNaughton, D., Robertson, E.G., Hathlerly, L.D. 1996, *J. Mol. Spectrosc.*, 175, 377
 Pascoli, G. & Lavendy, H. 1998, *Int. Jour. Mass. Spectr.*, 181, 11
 Pardo, J. R., Cernicharo, J., Serabyn, E. 2001, *IEEE Trans. Antennas and Propagation*, 49, 12
 Petrie, S. 1996, *MNRAS*, 281, 666
 Pickett, H.M., Poynter, R. L., Cohen, E. A., et al. 1998, *J. Quant. Spectrosc. Radiat. Transfer*, 60, 883
 Puzzarini, C. 2008, *Chem. Phys.*, 346, 45
 Saito, S., Kawaguchi, K., Yamamoto, S., et al. 1987, *ApJ*, 317, L115
 Tercero, F., López-Pérez, J. A., Gallego, et al., 2021, *A&A*, 645, A37
 Vastel, C., Quénard, D., Le Gal, R., et al. 2018, *MNRAS*, 478, 5514
 Vidal, T. H. G., Loison, J.-C., Jaziri, A. Y., et al. 2017, *MNRAS*, 469, 435
 Wakelam, V., Loison, J.-C., Herbst, E., et al. 2015, *ApJS*, 217, 20
 Wierzejewska, M., & Moc, J. 2003, *J. Phys. Chem. A*, 107, 11209
 Winnewisser, M., Schäfer, E. 1980, *Z. Naturforsch.*, 35a, 483
 Yamamoto, S., Saito, S., Kawaguchi, K., et al. 1987, *ApJ*, 317, L119

Appendix A: Column density and rotational temperature determination

In determining the column density of the molecules discovered and analysed in this work, we adopted a source of uniform brightness and 40'' radius (Fossé et al. 2001). We also adopted a full linewidth at half power intensity of 0.6 km s⁻¹, which represents a good average value to the linewidth of all observed lines in this work.

For the species with more than one line observed, we performed rotation diagrams to derive the corresponding rotational temperatures and column densities. However, for species for which we observed less than three transitions, we adopted the same source parameters and a rotational temperature of 10 K. In some cases we adopted the rotational temperature derived for a similar species. The different derived and/or adopted rotational temperatures for each species are given in Table 1 along with the derived column densities. For CS, HCS⁺, CCS, and C₃S, the column densities are taken from Cernicharo et al. (2021a). We note that the column density of CS, as its $J=1-0$ line has a significant optical depth, was derived from that of C³⁴S adopting the ³²S/³⁴S abundance ratio determined from C₃S and C₃³⁴S (24±3) (Cernicharo et al. 2021a). A similar result is obtained from ¹³C³⁴S adopting a ¹²C/¹³C abundance ratio of 90 (Cernicharo et al. 2020c). For all other molecules studied in this work, the lines are optically thin.

The error in getting column densities from the observed parameters of a single line and the assumed rotational temperature has been discussed in detail by Cernicharo et al. (2021a). In fact, the main source of uncertainty when the energy of the levels involved in the transition is $\leq T_K$ is not the assumed rotational temperature itself, but the assumption of it being uniform for all rotational levels (Cernicharo et al. 2021a). For example, changing the rotational temperature from 5 to 10 K for transitions $J=1-0$ or $J=2-1$ has a very modest effect on the column density (see, e.g. Cernicharo et al. 2021a and Cabezas et al. 2021). This is due to the fact that intensities are proportional to the rotational temperature T_r , but the partition function is inversely proportional to T_r for linear molecules. This also applies to asymmetric species with a large rotational constant A , which is much larger than T_r (H₂CCS and H₂CCCS, for example).

As a final check on the derived column densities, we also used the synthetic spectrum resulting from the best fit model to all lines of a molecule computed with the MADEx code (Cernicharo 2012). The final parameters derived this way should be very similar to those that could be derived from a standard rotation diagram. Nevertheless, this model fit allows one to compare the synthetic line profiles with observed ones, which is particularly interesting when the rotational transitions exhibit a hyperfine structure as is the case here for HCS, HSC, and HSCN, and to a lesser extent for HNCS.

Appendix B: Stacking spectra

For C₄S and C₅S, we observed several individual lines and their detection is solid. In order to provide additional support for it, we stacked the data following the procedure used recently to detect CH₃CH₂CCH in TMC-1 (Cernicharo et al. 2021c). The data were normalised to the expected intensity of each transition computed under local thermodynamic equilibrium (LTE) for the rotational temperature derived from the analysis of the individual lines. Finally, all the data were multiplied by the expected intensity of the strongest transition among the selected ones. The lines are optically thin, hence, the intensity of all lines scale in

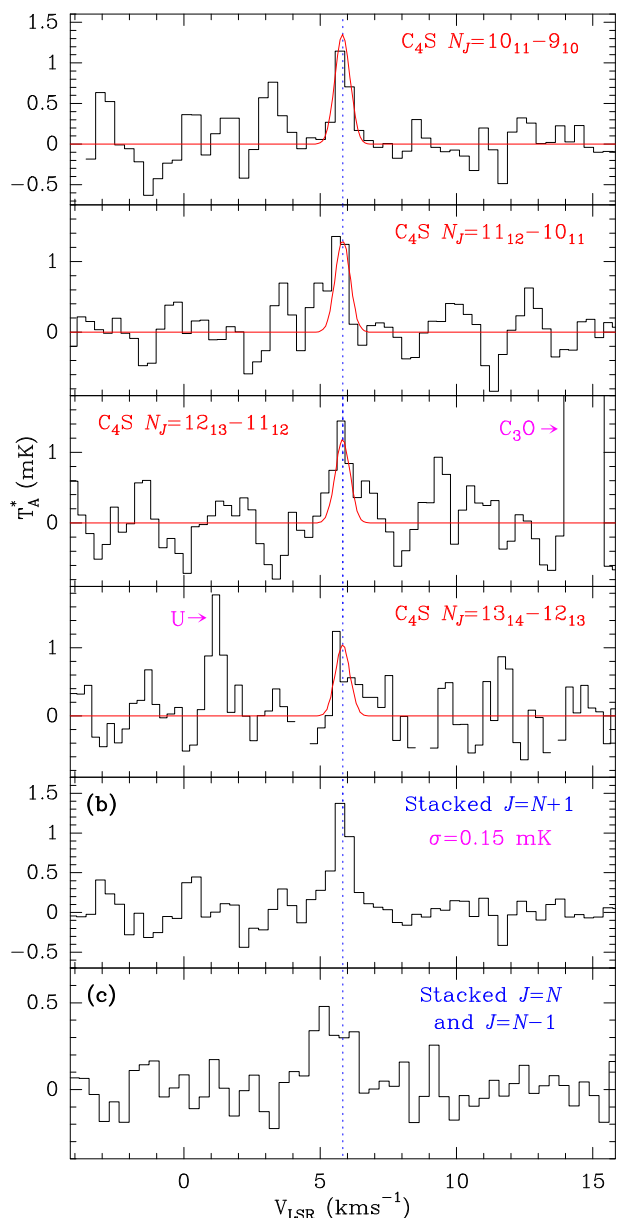


Fig. B.1. Four upper panels: Individual lines of C₄S with $J = N + 1$ detected in our survey. Two bottom panels: Spectrum obtained after stacking all lines of C₄S with $J = N + 1$ (panel b) and the resulting spectrum after stacking the twelve weak lines with $J = N$ and $J = N - 1$ (panel c). The abscissa corresponds to the velocity with respect to the local standard of rest. The dashed blue line corresponds to $v_{LSR}=5.83$ km s⁻¹. The ordinate is the antenna temperature in milliKelvin. The red line in the four upper panels corresponds to the synthetic spectrum for each transition computed with $T_r=7$ K and $N(C_4S)=3.8 \times 10^{10}$ cm⁻².

the same way with the assumed column density. Each individual spectra is weighted as $1/\sigma_N^2$, where σ_N now accounts for the normalisation intensity factor.

In order to strengthen the detection of C₄S, we grouped the observed lines into two different sets. The first one, with six lines, corresponds to the strongest transitions for $T_r=7$ K ($J=N+1$ transitions). A second group consists of thirteen lines corresponding to the weak $J = N$ and $J = N - 1$ transitions, which are 2-3 times weaker than those of the first group for the derived rotational temperature and, therefore, are below the 3σ detection limit for individual lines (~ 0.9 - 1.5 mK) in the observed frequency range. We again normalised all spectra to the

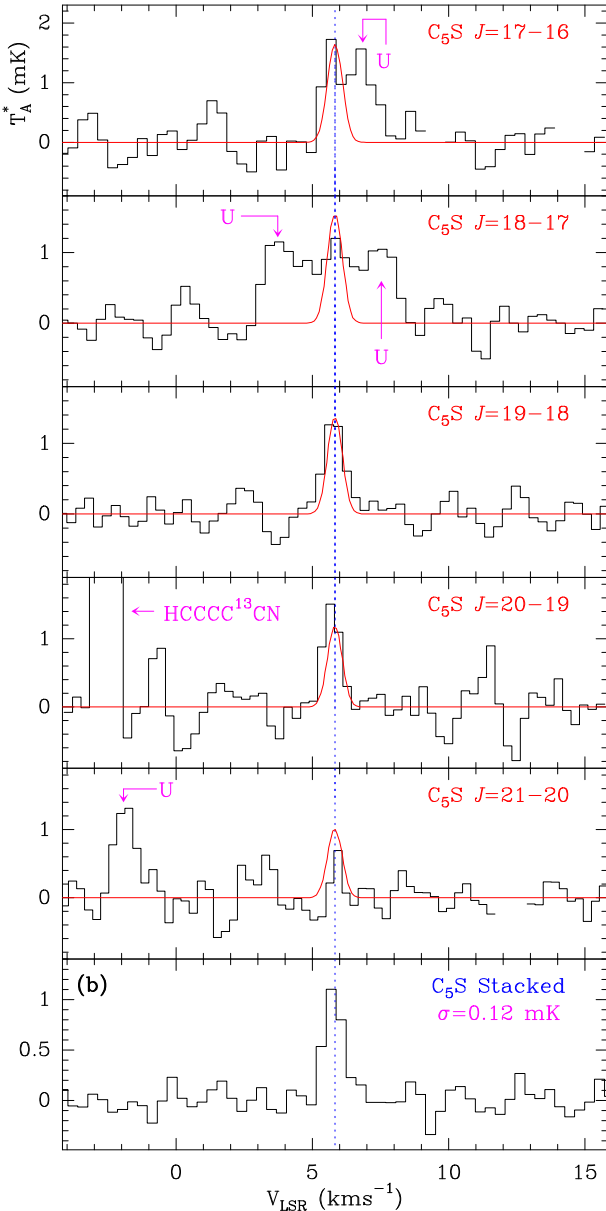


Fig. B.2. Detected lines of C_5S within the observed frequency range. The abscissa corresponds to the velocity with respect to the local standard of rest. The ordinate is the antenna temperature corrected for atmospheric and telescope losses in milliKelvin. Spectral resolution is 38.15 kHz. The dashed blue line corresponds to $v_{LSR}=5.83 \text{ km s}^{-1}$. The red line represents the synthetic spectrum for each line computed for $T_r=7 \text{ K}$ and $N(C_5S)=5 \times 10^{10} \text{ cm}^{-2}$. Panel (b) shows the stacked spectrum of all rotational transitions of C_5S in our survey from $J_u=17$ to 27.

predicted intensity of the strongest line ($N_J = 10_{11} - 9_{10}$) and averaged all the data in each set using the root mean square noise of each normalised spectrum as a weighting factor. We verified that none of these lines are contaminated by an unknown feature or from a transition of a known molecular species (it could appear centred on the local standard of rest velocity of the cloud). In all individual spectra, the emission from other features outside the expected velocity range was removed by blanking the channels (for example the line of C_3O in the $N_J = 12_{13} - 11_{12}$ spectrum; see Fig. B.1). Negative features due to the frequency switching folding were also eliminated before stacking the data. As quoted above, four of the six strongest lines are clearly detected (see Fig. B.1), and the other two do not show any significant emis-

sion at the expected velocity (their intensities are predicted to be 1.5-2 times weaker than the strongest transition). The stacked spectrum clearly shows a spectral feature at the expected velocity with a signal-to-noise ratio of ≈ 7 , as shown in panel *b* of Fig. B.1. For the group of thirteen weak lines, the resulting stacked spectrum is shown in panel *c* of the same figure. A line at 4σ is detected. Hence, the detection of the C_4S radical is robust.

For C_5S , the detection of five individual lines (see Fig. B.2) provides solid evidence on the detection of this species in TMC-1. The observed transitions have upper energy levels between 13 and 20 K. Three additional transitions above 40 GHz have intensities too low to be detected with the present sensitivity. Nevertheless, the stacked spectrum of all transitions results on a line at 8σ . Hence, we conclude that the detection of these two S-bearing carbon chains in TMC-1 is solid and convincing.

Appendix C: Abundances of related sulfur-bearing species

Appendix C.1: HCS and HSC

HCS and HSC were discovered by Agúndez et al. (2018) towards L483. Here, we present the first detection of these species in TMC-1. The observed lines are shown in Figures C.1 and C.2, respectively. Assuming a rotational temperature of 5 K, we derived $N(\text{HCS})=(5.5 \pm 0.5) \times 10^{12} \text{ cm}^{-2}$ and $N(\text{HSC})=(1.3 \pm 0.1) \times 10^{11} \text{ cm}^{-2}$. The column densities increase by $\sim 20\%$ if a rotational temperature of 10 K is assumed. The derived abundance ratio $X(\text{HCS})/X(\text{HSC})$ is 42 ± 7 , which is very similar to the value derived by Agúndez et al. (2018) towards L483. However, we derived an abundance ratio $\text{H}_2\text{CS}/\text{HCS}$ of ~ 9 , while in L483 this ratio is ~ 1 . Our purely gas-phase chemical model results in a $\text{H}_2\text{CS}/\text{HCS}$ ratio of ~ 200 (see Table 1) that is too high compared with the values observed in TMC-1 and L483, although the chemical model of Vidal et al. (2017), which includes grain-surface reactions, predicts a $\text{H}_2\text{CS}/\text{HCS}$ ratio close to the value observed in TMC-1. In the case of HCS and HSC, we could speculate with a common precursor, HCSH^+ . However, as discussed by Agúndez et al. (2018), the most stable isomer of this cation is H_2CS^+ and the formation of HSC from its dissociative recombination requires a substantial rearrangement of the molecular structure. If, as suggested by those authors that the CH_3S^+ cation is the common precursor of H_2CS and HCS, additional reactions are needed to explain the different $\text{H}_2\text{CS}/\text{HCS}$ abundance ratio found towards TMC-1 and L483.

Appendix C.2: SO, H_2CS , and OCS

We note that SO and NS do not have strong transitions in the 31-50 GHz domain; SO has one transition in this domain, the 3_2-2_2 , but its upper energy level is 21.1 K and we observed a weak emission feature at the correct frequency (see Table D.1). This line has peculiar excitation conditions as it turns out to be in absorption in front of the cosmic microwave background for low volume densities and in emission for the typical densities of TMC-1. Lique et al. (2006) studied SO in detail in this cloud and they derived an abundance of $\sim 10^{-8}$. Using the collisional rates of Lique et al. (2005), we derived a brightness temperature for the 3_2-2_2 transition of SO of -21, -17, 1.8, and 38 mK for $n(\text{H}_2)=10^4, 4 \times 10^4, 6 \times 10^4$, and 10^5 cm^{-3} , respectively. The predicted intensity has a direct dependency on the column density, but the turnover between absorption and emission essentially depends on the volume density. From the observed parameters for this line (see Table D.1) and the abundance derived by Lique et

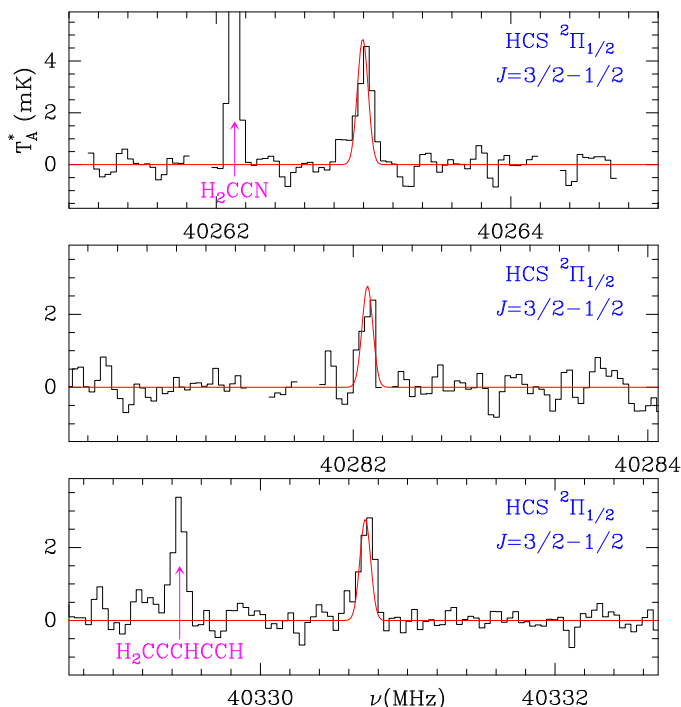


Fig. C.1. Observed lines of HCS within the observed frequency range. The abscissa corresponds to the rest frequency assuming a velocity with respect to the local standard of rest of 5.83 km s^{-1} . The ordinate is the antenna temperature corrected for atmospheric and telescope losses in milliKelvin. Spectral resolution is 38.15 kHz . The red line shows the synthetic spectrum for $T_r=5 \text{ K}$ and $N=(5.50\pm0.50)\times10^{12}$.

al. (2006), we estimate a volume density for the core of TMC-1 of $4\text{--}6\times10^4 \text{ cm}^{-3}$, which is in good agreement with previous studies (see, e.g. Fossé et al. 2001 and Lique et al. 2006). Assuming the H_2 column density derived by Cernicharo & Guélin (1987), the column density of SO is $\sim10^{14} \text{ cm}^{-2}$.

In our 7mm line survey, H_2CS only has one transition. Both, the main and the 34 isotopologues have been detected. Line parameters are given in Table D.1. The column density for this species was derived assuming a rotational temperature of 10 K (Cernicharo et al. 2021a).

It is important note that OCS has two transitions in the 31-50 GHz domain. Line parameters are given in Table D.1.

Appendix C.3: HNCS, HSCN, HCNS, and HSNC

We note that HNCS and HSCN have been previously detected in the interstellar medium (Frerking et al. 1979; Halfen et al. 2009). They are the sulfur equivalent of the well known molecules HNCO and HOCN; HNCS is the most stable among the possible CHNS isomers, with HSCN, HCSN, and HSNC being 3200, 17300, and 18100 K above HNCS, respectively (Wierzejewska & Moc 2003).

Adande et al. (2010) have already observed HSCN and HNCS in TMC-1. We observed the $3_{0,3}\text{--}2_{0,2}$ and $4_{0,4}\text{--}3_{0,3}$ transitions of both species, with the corresponding fine structure components for HSCN. The observed lines are shown in Fig. C.3. By performing a model fitting through the synthetic spectrum, we conclude that a rotational temperature in the range of 5-8 K produces a good match, although the best agreement is found for $T_r=5 \text{ K}$ (see Fig. C.3). We derived a column density of $(3.8\pm0.4)\times10^{11} \text{ cm}^{-2}$ for HNCS and $(5.8\pm0.6)\times10^{11} \text{ cm}^{-2}$ for HSCN. It seems that HSCN is slightly more abundant than

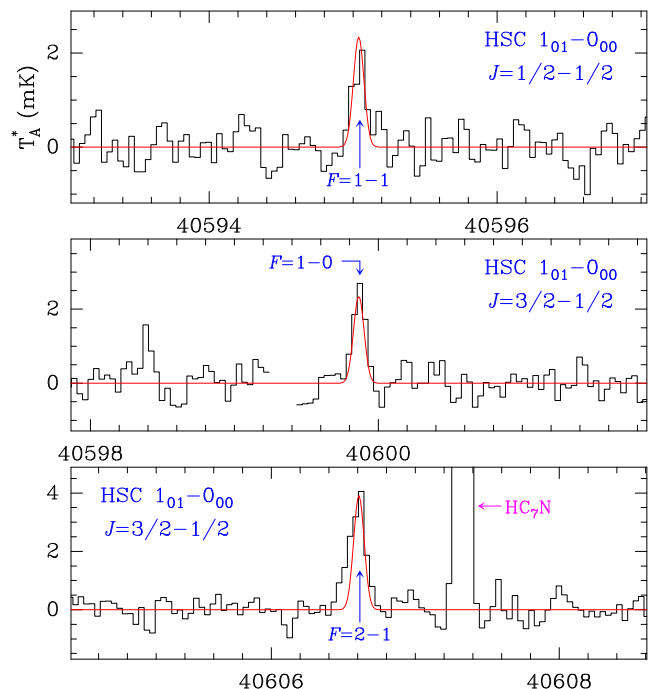


Fig. C.2. Observed lines of HSC within the observed frequency range. The abscissa corresponds to the rest frequency assuming a velocity with respect to the local standard of rest of 5.83 km s^{-1} . The ordinate is the antenna temperature corrected for atmospheric and telescope losses in milliKelvin. Spectral resolution is 38.15 kHz . The red line shows the synthetic spectrum for $T_r=5 \text{ K}$ and $N=(5.50\pm0.50)\times10^{12}$.

HNCS, despite being less stable, with an abundance ratio of $\text{HSCN}/\text{HNCS}=1.5\pm0.3$. The column densities of HNCS and HSCN derived by Adande et al. (2010) are somewhat lower than those derived here, although the ratio HSCN/HNCS derived by these authors is also around one.

The oxygen analogues HNCO and HOCN have a very different abundance ratio in TMC-1, where $\text{HNCO}/\text{HOCN}\sim130$ (Cernicharo et al. 2020c). The same behaviour is observed in warm molecular clouds, where HNCS and HSCN have comparable abundances, while HNCO is two orders of magnitude more abundant than HOCN (Adande et al. 2010). These authors argue that HSCN and HCSN could arise from a common precursor, HSCNH^+ , while HNCO may arise mostly from H_2NCO^+ . However, the uncertainties in the chemical networks regarding the chemistry of CHNO and CHNS isomers are still large. It is interesting to note that while in L483, the abundance ratio HNCO/NCO is ~5 (Marcelino et al. 2018), in TMC-1 the HNCS/NCS ratio is ~0.5 . This fact strengthens the different behaviour of the CHNO and CHNS systems in interstellar clouds.

We also searched for the two isomers HCNS and HSNC (thio and isothio fulminic acid, respectively) for which laboratory spectroscopy is available (McGuire et al. 2016). We derived a 3σ upper limit to their column density of $6\times10^{10} \text{ cm}^{-2}$ and $2\times10^{10} \text{ cm}^{-2}$, respectively.

Appendix C.4: HCCSH, HCCCSH, and HSCS⁺

We note that HCCSH is a metastable isomer, with an energy of 6770 K above the most stable isomer H_2CCS (Lee et al. 2019). It has been searched for towards several sources (McGuire et al. 2019), but only upper limits have been obtained for its abundance. In TMC-1, McGuire et al. (2019) derived a 1σ upper limit to its column density of $\leq2.9\times10^{13} \text{ cm}^{-2}$. In our Q-band

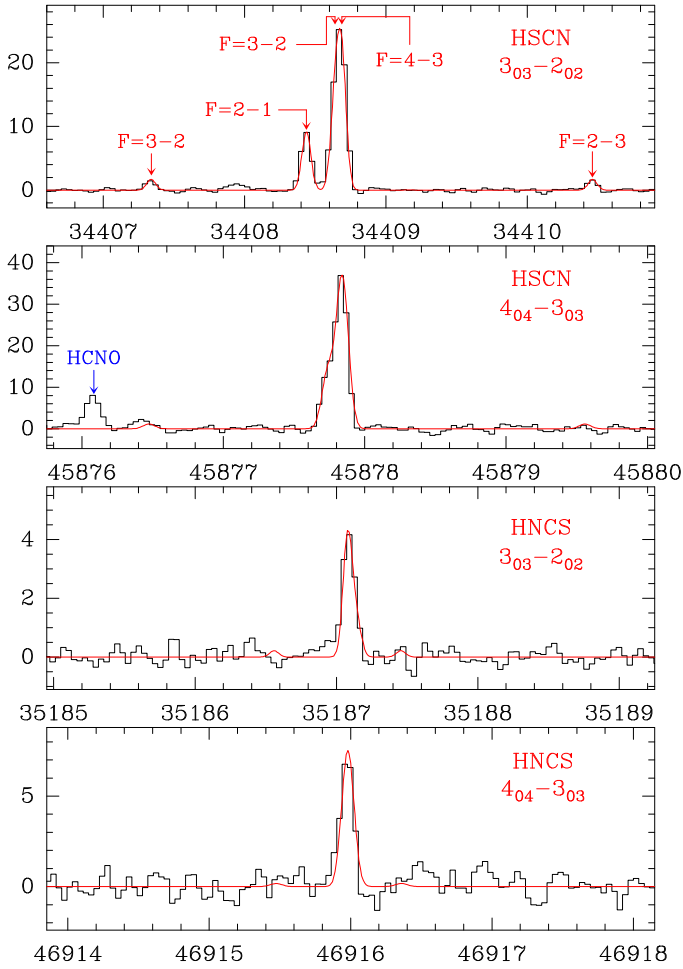


Fig. C.3. Observed lines of HSCN and HNCS within the observed frequency range. The abscissa corresponds to the rest frequency assuming a velocity with respect to the local standard of rest of 5.83 km s^{-1} . The ordinate is the antenna temperature corrected for atmospheric and telescope losses in milliKelvin. Spectral resolution is 38.15 kHz . The red line shows the synthetic spectrum for $T_r=5 \text{ K}$ and $N=(5.80\pm0.60)\times10^{11} \text{ cm}^{-2}$ for HSCN, and $N=(3.80\pm0.40)\times10^{11} \text{ cm}^{-2}$ for HNCS.

data, we have searched for the lines of this species. Assuming a rotational temperature of 7 K , we derived a 3σ upper limit of $N\leq9\times10^{12} \text{ cm}^{-2}$. The rather poor upper limit is due to its low μ_a dipole moment $\mu_a=0.13 \text{ D}$ (Lee et al. 2019). The b component of the dipole moment is larger, but b -type transitions for this species are outside the frequency range of our survey and they involve energy levels that will be unpopulated under the physical conditions of TMC-1.

We also searched for HCCCSH, an isomer of H_2CCCS , which is predicted to lie around 1000 K above it (Brown et al. 1982; Crabtree et al. 2016), but only a 3σ upper limit to its column density of $2.4\times10^{11} \text{ cm}^{-2}$ was obtained (see Table 1). It is interesting to note that in TMC-1, the abundance ratio $\text{HCCCHO}/\text{H}_2\text{CCCO}$ is well above one (Loison et al. 2016; Cernicharo et al. 2020c), while the $\text{HCCCSH}/\text{H}_2\text{CCCS}$ ratio is found to be below one.

Finally, we have also searched for HSCS^+ (McCarthy et al. 2009), the protonated form of carbon disulfide. Due to its low dipole moment (McCarthy et al. 2009), the derived 3σ upper limit for its column density is $\leq3.0\times10^{12} \text{ cm}^{-2}$ (average result from the four lines in our survey).

Appendix D: Line parameters

Line parameters for all observed transitions were derived by fitting a Gaussian line profile to them. A velocity range of $\pm20 \text{ km s}^{-1}$ around each feature was considered for the fit after a polynomial baseline was removed. The derived line parameters are given in Table D.1.

Table D.1. Observed line parameters for sulfur-bearing species in TMC-1.

Transition	ν_{rest}^a (MHz)	$\int T_A^* dv^b$ (mK km s ⁻¹)	ν_{LSR}^c (km s ⁻¹)	$\Delta\nu^d$ (km s ⁻¹)	T_A^{*e} (mK)
HCCS					
7/2-5/2 4-3*	41077.779±0.001	3.6±0.5	5.71±0.02	0.71±0.06	4.8±0.3
7/2-5/2 3-2*	41078.876±0.001	2.3±0.5	5.72±0.03	0.54±0.07	3.4±0.3
H₂CS					
1 ₀₁ – 0 ₀₀	34351.430±0.001	413.2±5.6	5.85±0.01	0.75±0.01	518.1±0.3
3 ₀₃ – 2 ₀₂	103040.447±0.001	577.9±9.8	5.80±0.01	0.54±0.01	1010.7±2.6
3 ₁₃ – 2 ₁₂	101477.805±0.001	583.4±9.9	5.78±0.01	0.54±0.01	1017.0±2.5
3 ₁₂ – 2 ₁₁	104617.027±0.001	523.1±9.5	5.80±0.01	0.54±0.01	905.7±2.2
H₂C³⁴S					
1 ₀₁ – 0 ₀₀	33765.750±0.001	17.4±0.8	5.73±0.01	0.77±0.03	21.2±0.4
3 ₀₃ – 2 ₀₂	101284.314±0.001	22.2±2.0	5.78±0.01	0.52±0.02	40.0±2.4
3 ₁₃ – 2 ₁₂	99774.077±0.001	23.8±1.3	5.74±0.01	0.55±0.02	44.0±1.4
3 ₁₂ – 2 ₁₁	102807.337±0.001	19.8±2.8	5.74±0.02	0.53±0.05	34.9±3.0
H₂CCS					
3 ₁₃ – 2 ₁₂	33438.371±0.003	1.3±0.3	5.91±0.04	0.65±0.08	1.8±0.3
3 ₁₂ – 2 ₁₁	33783.257±0.003	1.9±0.3	5.85±0.04	0.78±0.08	2.3±0.3
4 ₁₄ – 3 ₁₃	44584.335±0.004	1.7±0.3	5.93±0.04	0.55±0.08	2.9±0.4
4 ₁₃ – 3 ₁₂	45044.177±0.004	2.5±0.4	5.87±0.04	0.69±0.09	3.5±0.4
7 ₁₇ – 6 ₁₆	78021.269±0.006	5.0±1.0	5.87±0.05	0.32±0.08	14.5±3.8
7 ₁₆ – 6 ₁₅	78825.943±0.006				≤8.4 ^f
3 ₀₃ – 2 ₀₂	33611.707±0.001	1.5±0.4	5.73±0.07	1.03±0.10	1.4±0.3
4 ₀₄ – 3 ₀₃	44815.323±0.002	1.4±0.4	5.81±0.05	0.67±0.12	2.0±0.3
H₂CCCS					
7 ₁₇ – 6 ₁₆	35300.943±0.007	3.0±0.3	5.78±0.02	0.86±0.05	3.3±0.2
7 ₁₆ – 6 ₁₅	35466.111±0.007	2.3±0.3	5.88±0.03	0.67±0.07	3.3±0.3
8 ₁₈ – 7 ₁₇	40343.856±0.008	3.0±0.4	5.83±0.02	0.60±0.05	4.8±0.3
8 ₁₇ – 7 ₁₆	40532.618±0.008	3.5±0.4	5.92±0.02	0.64±0.04	5.1±0.3
9 ₁₉ – 8 ₁₈	45386.736±0.009	3.9±0.5	5.84±0.03	0.60±0.08	4.6±0.4
9 ₁₈ – 8 ₁₇	45599.094±0.009	3.3±0.5	5.97±0.06	0.84±0.18	3.7±0.7
7 ₀₇ – 6 ₀₆	35384.411±0.006	1.0±0.3	5.89±0.05	0.64±0.10	1.4±0.3
8 ₀₈ – 7 ₀₇	40439.230±0.009	1.2±0.3	5.74±0.06	0.62±0.09	1.8±0.3
9 ₀₉ – 8 ₀₈	45494.010±0.009	1.2±0.4	5.92±0.10	0.73±0.13	1.5±0.5
C₄S					
10 ₁₁ – 9 ₁₀	32553.160±0.006	0.8±0.3	5.82±0.07	0.63±0.19	1.2±0.3
11 ₁₂ – 10 ₁₁	35519.754±0.009	0.9±0.4	5.74±0.07	0.51±0.22	1.7±0.3
12 ₁₃ – 11 ₁₂	38488.028±0.011	1.2±0.4	5.76±0.07	0.85±0.21	1.4±0.3
13 ₁₄ – 12 ₁₃	41458.049±0.014	0.7±0.3	5.70±0.15	0.45±0.20	1.5±0.3
C₅S					
17-16	31371.640±0.010	0.9±0.3	5.65±0.14	0.55±0.15	1.6±0.3
18-17	33216.995±0.012	0.9±0.4	5.78±0.20	0.90±0.25	1.0±0.3
19-18	35062.344±0.014	1.1±0.4	5.81±0.07	0.80±0.25	1.2±0.4
20-19	36907.686±0.017	0.7±0.3	5.73±0.10	0.59±0.14	1.1±0.4
21-20	38753.022±0.020	0.4±0.3	5.80±0.10	0.55±0.24	0.8±0.4
HNCS					
3 ₀₃ – 2 ₀₂	35187.110±0.020	3.7±0.8	6.04±0.03	0.86±0.05	4.0±0.3
4 ₀₄ – 3 ₀₃	46916.000±0.020	5.4±1.0	6.01±0.02	0.70±0.05	7.3±0.6
7 ₀₇ – 6 ₀₆	82101.824±0.002	5.5±1.0	5.89±0.04	0.43±0.08	12.0±2.4
8 ₀₈ – 7 ₀₇	93830.050±0.020	3.5±1.0	5.83±0.05	0.47±0.11	7.1±1.9
9 ₀₉ – 7 ₀₇	105558.074±0.020	3.7±1.0	5.98±0.04	0.30±0.08	11.7±3.5
HSCN					
3 ₀₃ – 2 ₀₂ 3-2 + 4-3	34408.664±0.003	25.2±0.4	5.86±0.01	0.92±0.01	25.5±0.3

Table D.1. continued.

Transition	ν_{rest}^a (MHz)	$\int T_A^* dv^b$ (mK km s ⁻¹)	ν_{LSR}^c (km s ⁻¹)	$\Delta\nu^d$ (km s ⁻¹)	T_A^{*e} (mK)
3 ₀₃ – 2 ₀₂ 2-1	34408.437±0.003	7.2±0.4	5.95±0.01	0.75±0.03	9.0±0.3
3 ₀₃ – 2 ₀₂ 2-2	34410.461±0.003	1.5±0.4	6.00±0.05	0.78±0.12	1.8±0.3
3 ₀₃ – 2 ₀₂ 2-2	34407.339±0.003	0.9±0.3	6.00±0.08	0.66±0.14	1.4±0.3
4 ₀₄ – 3 ₀₃ 4-3 + 5-4	45877.823±0.004	24.7±1.5	5.80±0.02	0.63±0.03	36.8±0.8
4 ₀₄ – 3 ₀₃ 3-2	45877.736±0.004	9.8±1.6	5.90±0.05	0.68±0.09	13.4±0.8
7 ₀₇ – 6 ₀₆	80823.192±0.007	16.1±2.5	5.88±0.02	0.57±0.05	26.3±2.7
8 ₀₈ – 7 ₀₇	91750.662±0.008	13.3±2.6	5.95±0.03	0.68±0.07	18.5±2.4
HCS					
1 ₀₁ – 0 ₀₀ 3/2-1/2 2-1	40262.996±0.005	3.5±1.0	5.67±0.08	0.76±0.18	4.3±0.3
2 ₀₂ – 1 ₀₁ 5/2-3/2 3-2	80553.516±0.004	6.2±1.0	5.64±0.03	0.34±0.07	17.0±2.9
2 ₀₂ – 1 ₀₁ 5/2-3/2 2-1	80565.596±0.004	6.2±1.0	5.77±0.07	0.63±0.16	9.3±2.9
2 ₀₂ – 1 ₀₁ 5/2-3/2 2-1	80596.409±0.003	3.3±1.0	5.64±0.05	0.28±0.08	11.3±2.7
HSC					
1 ₀₁ – 0 ₀₀ 1/2-1/2 0-1	40584.337±0.003	1.2±0.3	5.50±0.06	0.58±0.13	1.9±0.3
1 ₀₁ – 0 ₀₀ 1/2-1/2 1-1	40595.040±0.003	1.6±0.4	5.79±0.07	0.88±0.18	1.7±0.3
1 ₀₁ – 0 ₀₀ 1/2-1/2 1-0	40599.864±0.003	2.2±0.4	5.81±0.04	0.76±0.09	2.7±0.3
1 ₀₁ – 0 ₀₀ 1/2-1/2 2-1	40606.608±0.003	4.0±0.5	5.90±0.04	1.05±0.09	3.6±0.3
OCS					
4-3	36488.812±0.000	25.9±0.5	5.88±0.01	0.83±0.01	29.3±0.3
5-4	48651.604±0.000	32.1±0.5	5.91±0.01	0.76±0.01	39.7±0.7
OC³⁴S					
4-3	35596.869±0.000	1.1±0.4	5.85±0.09	0.92±0.17	1.2±0.3
5-4	47762.353±0.000				≤2.1 ^f
SO					
3 ₂ – 2 ₂	36202.034±0.002	1.3±0.0	6.16±0.05	0.70±0.10	1.7±0.3

Notes.

^(a) Predicted frequencies from the MADEX code (Cernicharo 2012). For lines with zero uncertainty for the velocity, the frequency corresponds to the measured one assuming ν_{LSR} 5.83 km s⁻¹.

^(b) Integrated line intensity in milliKelvin km s⁻¹.

^(c) Line velocity with respect to the local standard of rest in km s⁻¹. If the associated uncertainty is equal to zero, then the velocity has been fixed to 5.83 km s⁻¹.

^(d) Linewidth at half intensity derived by fitting a Gaussian line profile to the observed transitions (in km s⁻¹).

^(e) Antenna temperature in milliKelvin.

^(f) 3 σ upper limit in mK.

^(*) Average of the *e* and *f* components which are separated by 33 kHz.

Appendix E: New reactions included

Table E.1. Reactions involving S-bearing species not included in either the chemical network UMIST RATE12 or that of Vidal et al. (2017).

Reaction	α (cm ³ s ⁻¹)	β	γ (K)	Type	Reference
NCS chemistry					
CN + S ₂ → NCS + S	2.02×10^{-11}	-0.19	-31.9	1	(CN + O ₂)
CN + SO → NCS + O	2.02×10^{-11}	-0.19	-31.9	1	(CN + O ₂)
N + HCS → NCS + H	1.00×10^{-10}	0.00	0	1	(N + HCO)
O + NCS → CO + NS	1.00×10^{-10}	0.00	0	1	(O + OCN)
H + NCS → SH + CN	1.00×10^{-10}	0.00	0	1	(H + OCN)
C + NCS → CS + CN	1.00×10^{-10}	0.00	0	1	(C + OCN)
H ₃ ⁺ + NCS → HNCS ⁺ + H ₂	0.50	3.47×10^{-9}	2.92	2	(H ₃ ⁺ + HNCS)
H ₃ ⁺ + NCS → HSCN ⁺ + H ₂	0.50	3.47×10^{-9}	2.92	2	(H ₃ ⁺ + HNCS)
HCO ⁺ + NCS → HNCS ⁺ + CO	0.50	1.32×10^{-9}	2.92	2	(HCO ⁺ + HNCS)
HCO ⁺ + NCS → HSCN ⁺ + CO	0.50	1.32×10^{-9}	2.92	2	(HCO ⁺ + HNCS)
HNCS ⁺ + H ₂ → H ₂ NCS ⁺ + H	1.51×10^{-9}	0.00	0	1	(HNCO ⁺ + H ₂)
HNCS ⁺ + H ₂ → HNCSH ⁺ + H	1.51×10^{-9}	0.00	0	1	(HNCO ⁺ + H ₂)
HSCN ⁺ + H ₂ → H ₂ SCN ⁺ + H	1.51×10^{-9}	0.00	0	1	(HOCN ⁺ + H ₂)
HSCN ⁺ + H ₂ → HNCSH ⁺ + H	1.51×10^{-9}	0.00	0	1	(HOCN ⁺ + H ₂)
C ₅ S chemistry					
HC ₃ S ⁺ + e ⁻ → C ₅ S + H	1.00×10^{-7}	-0.50	0	1	(HC ₃ S ⁺ + e ⁻)
HC ₃ S ⁺ + e ⁻ → C ₄ H + CS	1.00×10^{-7}	-0.50	0	1	(HC ₃ S ⁺ + e ⁻)
HC ₃ S ⁺ + e ⁻ → C ₄ S + CH	1.00×10^{-7}	-0.50	0	1	(HC ₃ S ⁺ + e ⁻)
C ₄ H + CS → C ₅ S + H	2.00×10^{-10}	0.00	0	1	(C ₂ H + CS)
S + C ₅ H → CS + C ₄ H	7.00×10^{-11}	0.00	0	1	(S + C ₃ H)
S + C ₅ H → C ₅ S + H	3.00×10^{-11}	0.00	0	1	(S + C ₃ H)
C + C ₅ S → C ₅ + CS	3.00×10^{-10}	0.00	0	1	(C + C ₃ S)
H ₃ ⁺ + C ₅ S → HC ₃ S ⁺ + H ₂	1.00	4.29×10^{-9}	4.39	2	(H ₃ ⁺ + C ₃ S)
H ₃ O ⁺ + C ₅ S → HC ₃ S ⁺ + H ₂ O	1.00	1.88×10^{-9}	4.39	2	(H ₃ O ⁺ + C ₃ S)
HCO ⁺ + C ₅ S → HC ₃ S ⁺ + CO	1.00	1.61×10^{-9}	4.39	2	(HCO ⁺ + C ₃ S)
C ⁺ + C ₅ S → C ₅ S ⁺ + C	0.25	2.28×10^{-9}	4.39	2	(C ⁺ + C ₃ S)
C ⁺ + C ₅ S → C ₆ ⁺ + S	0.25	2.28×10^{-9}	4.39	2	(C ⁺ + C ₃ S)
C ⁺ + C ₅ S → C ₅ + CS	0.25	2.28×10^{-9}	4.39	2	(C ⁺ + C ₃ S)
C ⁺ + C ₅ S → C ₅ + CS ⁺	0.25	2.28×10^{-9}	4.39	2	(C ⁺ + C ₃ S)
Miscellaneous					
H ₃ ⁺ + H ₂ C ₃ S → H ₃ C ₃ S ⁺ + H ₂	1.00	4.10×10^{-9}	2.37	2	KIDA
HCO ⁺ + H ₂ C ₃ S → H ₃ C ₃ S ⁺ + CO	1.00	1.53×10^{-9}	2.37	2	KIDA
H ₃ C ₃ S ⁺ + e ⁻ → H ₂ C ₃ S + H	4.00×10^{-8}	-0.70	0	1	KIDA
H ₃ C ₃ S ⁺ + e ⁻ → HC ₃ S + H + H	2.00×10^{-7}	-0.70	0	1	KIDA
H ₃ C ₃ S ⁺ + e ⁻ → CS + C ₂ H ₂ + H	2.00×10^{-7}	-0.70	0	1	KIDA
H ₃ C ₃ S ⁺ + e ⁻ → H ₂ CCC + SH	2.00×10^{-7}	-0.70	0	1	KIDA
C ⁺ + H ₂ C ₃ S → C ₃ H + HCS ⁺	1.00	2.17×10^{-9}	2.37	2	KIDA
C + H ₂ C ₃ S → CS + C ₃ H ₂	3.00×10^{-10}	0.00	0	1	KIDA
S + CH ₂ CCH → H ₂ C ₃ S + H	1.00×10^{-10}	0.00	0	1	KIDA
S + CH ₂ CCH → CS + C ₂ H ₃	2.00×10^{-11}	0.00	0	1	KIDA
S + CH ₂ CCH → HCS + C ₂ H ₂	2.00×10^{-11}	0.00	0	1	KIDA
H ₃ ⁺ + HCCS → H ₂ C ₂ S ⁺ + H ₂	1.00	2.90×10^{-9}	2.39	2	(H ₃ ⁺ + H ₂ CCS)
HCO ⁺ + HCCS → H ₂ C ₂ S ⁺ + CO	1.00	1.17×10^{-9}	2.39	2	(HCO ⁺ + H ₂ CCS)

Notes.

- For reactions of type 1, the rate coefficient is given by the expression $k(T) = \alpha (T/300)^\beta \exp(-\gamma/T)$.
- For reactions of type 2, the rate coefficient is given by the expression $k(T) = \alpha \beta (0.62 + 0.4767 \gamma \sqrt{300/T})$.
- Reactions from the KIDA database can be found at <http://kida.astrophy.u-bordeaux.fr/>.